EES Catalysis

PAPER

Check for updates

Single-atomic rhenium-assisted 2H-to-1T phase transformation of MoS2 nanosheets boosting electrocatalytic hydrogen evolution†

Jianmin Yu,‡[ac] Yongteng Qian, (iD) ‡[d] Qing Wang,[a] Chenliang Su, (iD)[c] Hyoyoung Lee, (iD)*[ef] Lu Shang (iD)*[a] and Tierui Zhang (iD)*[ab]

Metallic (1T) molybdenum disulfide (MoS2) with high electronic conductivity has been recognized as a promising catalytic material for the hydrogen evolution reaction (HER). However, there are still some challenges in obtaining high-degree and stable 1T-MoS2 due to its thermodynamically metastable characteristics. Here, we reported the single-atomic rhenium (Re)-assisted 2H-to-1T phase transformation (ca. 85%) of MoS2 nanosheets using a simple one-pot hydrothermal method. The resulting single-atomic Re doped 1T-2H MoS2 heterostructures delivered small overpotentials of 34 and 38 mV at a current density of 10 mA cm^{-2} in acid and alkaline media, respectively. Structural characterization and theoretical calculations indicate that the implantation of the Re single atom not only promotes the phase transition of MoS2 from the 2H to 1T phase and charge redistribution through the constructed Re–S–Mo site but also the additional Re single atom acts as the active site to facilitate the dissociation of water and the adsorption of the hydrogen intermediate. All these factors effectively improve the electrocatalytic properties of MoS2 for the HER.

Broader context

Single-atomic Re doped 1T-2H MoS2 heterostructures were successfully synthesized using a simple hydrothermal method. The as-prepared Re doped 1T-2H MoS2 heterostructures delivered small overpotentials of 34 and 38 mV at a current density of 10 mA cm^{-2} in acid and alkaline media, respectively. Our work demonstrates that the introduction of the Re single-atom is a facile method to realize the 2H-to-1T phase transition of MoS2, resulting in highly durable and efficient electrocatalysts for hydrogen evolution.

Introduction

Hydrogen is considered as one of the most promising energy carriers to replace fossil fuels due to its high energy density,

[a] Key Laboratory of Photochemical Conversion and Optoelectronic Materials, Technical Institute of Physics and Chemistry, Chinese Academy of Sciences, Beijing 100190, China. E-mail: lushang@mail.ipc.ac.cn, tierui@mail.ipc.ac.cn

[b] Center of Materials Science and Optoelectronics Engineering, University of Chinese Academy of Sciences, Beijing 100049, China

[c] International Collaborative Laboratory of 2D Materials for Optoelectronic Science and Technology of Ministry of Education, Institute of Microscale Optoelectronics, Shenzhen University, Shen Zhen, 518060, China

[d] Department of Physics and Interdisciplinary Course of Physics and Chemistry, Sungkyunkwan University (SKKU), Suwon 16419, Republic of Korea

[e] Center for Integrated Nanostructure Physics, Institute for Basic Science (IBS), Sungkyunkwan University, Suwon, 16419, Republic of Korea

[f] Department of Chemistry, Sungkyunkwan University (SKKU), Suwon 16419, Republic of Korea. E-mail: hyoyoung@skku.edu

† Electronic supplementary information (ESI) available: Experimental section. See DOI: https://doi.org/10.1039/d3ey00037k

‡ J. Y. and Y. Q. contributed equally to this work.

cleanliness, and renewability.[1] Electrocatalytic water splitting driven by green electricity (such as solar cells) represents a potential environment-friendly approach for large-scale hydrogen generation.[2] The hydrogen evolution reaction (HER) is crucial in water electrolysis. Noble-metal-based materials (such as Pt-based materials) with suitable Gibbs-free energies for H adsorption have displayed superior HER performance.[3,4] However, it is widely concerning that their high cost and scarcity are seriously impeding their industrial applications. Therefore, it is important to develop HER electrocatalysts with excellent performance at low cost.[5]

During the past several years, two-dimensional (2D) transition metal dichalcogenides (TMD) have been considered as a promising alternative catalytic material due to their unique electronic and physical properties, such as atomic-scale thickness, strong spin–orbit coupling, and direct band gap.[6,7] In particular, 2D TMD materials with a metallic 1T phase are usually regarded as favorable for catalyzing electrochemical hydrogen production from water compared with other phases

due to the following merits: firstly, the higher electrical conductivity supplied better charge transport capability.[8] Secondly, both basal planes and edges of the 1T phase can be activated for hydrogen adsorption rather than just the edges of the 2H phase.[9] In recent years, many works have attempted to promote the accessibility of the 2H-to-1T phase transformation. The typical synthesis approaches of metallic 1T-MoS$_2$ involved alkali–ion intercalation,[10] external irradiation,[11] micromechanical exfoliations,[12] and thermal treatment.[13] Nevertheless, the thermodynamic instability of the 1T phase of TMD still impedes its practical application.[8,14] To overcome this limitation, heteroatom doping as a prevalent strategy has been applied to stabilize the metallic 1T phase. For example, Ir-doped,[15] Rh-doped,[16] or (Pd, Ru)-co-doped,[17] either trigger metallic 1T or activate the inert plane to elevate the catalytic performance of pristine MoS$_2$. Besides that, phase engineering with the incorporation of single atoms (SA) is also another important strategy, similar to heteroatom doping, which speculated that the large quantities of active sites and the intrinsic activity of each existing active site would afford an increase in the performance and stability of the HER.[18] For instance, single-atom Ru supported on MoS$_2$ as an alternative electrocatalyst to produce the stable 1T-phase MoS$_2$ with a S-vacancy formation has been proposed for an excellent HER.[19] In another example, the synergistic strategy of phase conversion engineering and incorporation of Pt single atoms into the MoS$_2$ lattice was reported, which can convert the 2H-phase to the 1T-phase via a potential cycling method and enhance the performance of inert 2D MoS$_2$ for the HER.[20]

Rhenium (Re), as a 5d transition metal, is close to the Pt group, but its price is much less than that of the noble metals (Pt, Ir, and Pd).[21,22] What's more, Re possesses a similar radius and a different number of valence electrons compared with Mo, which is emerging as a suitable dopant to induce phase transition of 2D TMD.[23,24] Herein, the 2H-to-1T phase transformation of MoS$_2$ was successfully realized by introducing Re SA into MoS$_2$ (Re–SA/MoS$_2$) through a facile hydrothermal method. The optimized Re–SA/MoS$_2$ showed excellent catalytic activity for the HER with small overpotentials of 34 and 38 mV at 10 mA cm^{-2} in acidic and alkaline electrolytes, respectively. Moreover, the optimized Re–SA/MoS$_2$ also presents good stability for hydrogen evolution in both acidic and alkaline electrolytes. The density functional theory (DFT) results demonstrated that the injection of the Re SA into MoS$_2$ can significantly adjust the electronic structure, optimize the adsorption-free energy of the MoS$_2$, and further enhance the catalytic kinetics. This work demonstrates that the introduction of a Re single-atom is a facile method to realize the 2H-to-1T phase transition of MoS$_2$ and thereby produces durable and efficient electrocatalysts for hydrogen evolution.

Results and discussion

Synthesis and structural characterization of Re–SA/MoS$_2$ nanosheets

As depicted in Fig. 1a, the Re–SA/MoS$_2$ nanosheets were synthesized on carbon cloth using a hydrothermal method.

Phase identification and crystallinity in pristine MoS$_2$ and Re–SA/MoS$_2$ were investigated by the corresponding X-ray diffraction (XRD) patterns (Fig. 1b). The prominent diffraction peaks at 14.5° and 33.5° could be ascribed to the (002) and (101) facets of the 2H-phase MoS$_2$ (JCPDS No. 65-0160). With the addition of Re ions, the (002) facets of Re–SA/MoS$_2$ shifted to lower 2θ values compared with the pristine MoS$_2$ (Fig. S1, ESI†), which indicates the Re SA were successfully doped into the lattice of MoS$_2$.[25] Scanning electron microscopy (SEM) images (Fig. S2, ESI†) and transmission microscopy (TEM) images (Fig. 1c and Fig. S3a–c, ESI†) revealed that both MoS$_2$ and Re–SA/MoS$_2$ possessed a typical flower-like nanosheet structure. Moreover, compared with MoS$_2$, the surfaces of Re–SA/MoS$_2$ were rougher and the size of the Re–SA/MoS$_2$ nanosheets had a significant reduction in the lateral diameter, implying that the nanosheet morphology of Re–SA/MoS$_2$ was retained after the introduction of the Re SA.[25] From the high-resolution TEM (HRTEM) images (Fig. 1d), the lattice fringe distance of 0.69 nm corresponding to the (002) planes of Re–SA/MoS$_2$ is slightly larger than that of pristine MoS$_2$ (0.65 nm) (Fig. S3d, ESI†), reflecting a lattice expansion after incorporation of the Re SA, which is consistent with the XRD observation. The images of energy dispersive X-ray spectrometry (EDS) elemental mapping (Fig. 1e and Fig. S3e, ESI†) proved a homogeneous distribution of the Re SA over the MoS$_2$ nanosheets.

To further validate the 2H to 1T phase conversion of MoS$_2$ and the atomic dispersion of Re sites in Re–SA/MoS$_2$, aberration-corrected high-angle annular dark-field scanning transmission electron microscopy (HAADF-STEM) was performed. As illustrated in Fig. 2a and b, the average (101) interlayer spacing with $\sim$0.27 nm and a unique honeycomb-like structure are displayed in MoS$_2$. However, the averaged (101) interlayer spacing of Re–SA/MoS$_2$ increased to 0.29 nm (Fig. 2c), corresponding to the probable existence of the surface tensile strain from the ambient Re atoms.[26] The magnified HAADF-STEM images (Fig. 2b and d) combined with the indicated line 1 and 2 profiles (Fig. 2e) exhibited that a natural atomic pattern of 2H-phase MoS$_2$ is Mo–S–Mo, but 1T-phase MoS$_2$ shows a distinct atomic pattern of the two S atoms between neighboring Mo atoms, confirming that the crystal phase of MoS$_2$ was transformed into the 1T-phase in Re–SA/MoS$_2$. Importantly, the existence of the isolated bright dots was marked by yellow circles (Fig. 2c and d), indicating that the Re sites were dispersed in the MoS$_2$ in the form of single atoms.[27] Further direct evidence was corroborated by the intensity profile collected at line 3 (Fig. 2e), where the higher HAADF intensity of the third atom is observable, indicating that the heavier Re SA ($Z = 75$) were possibly anchored to the surface of MoS$_2$ (referred to as "adsorption") or substituted the lighter Mo atom ($Z = 42$).[28,29] Raman spectroscopy was also applied to further distinguish the lattice structure of the 1T-phase and 2H-phase of MoS$_2$.[30] As shown in Fig. 2f, the bands located at 378 cm^{-1} and 404 cm^{-1} could be indexed as the in-plane E$_{2g}^1$ vibration mode and the out-of-plane A$_{1g}$ vibration mode of 2H-MoS$_2$. In contrast, the new prominent bands at 146 cm^{-1}, 196 cm^{-1}, 283 cm^{-1}, and 337 cm^{-1} were attributed to the J_1, J_2, E$_{1g}$, and J_3 of 1T-phase of MoS$_2$ in the Re–SA/MoS$_2$ nanosheets, which confirmed that spontaneous phase
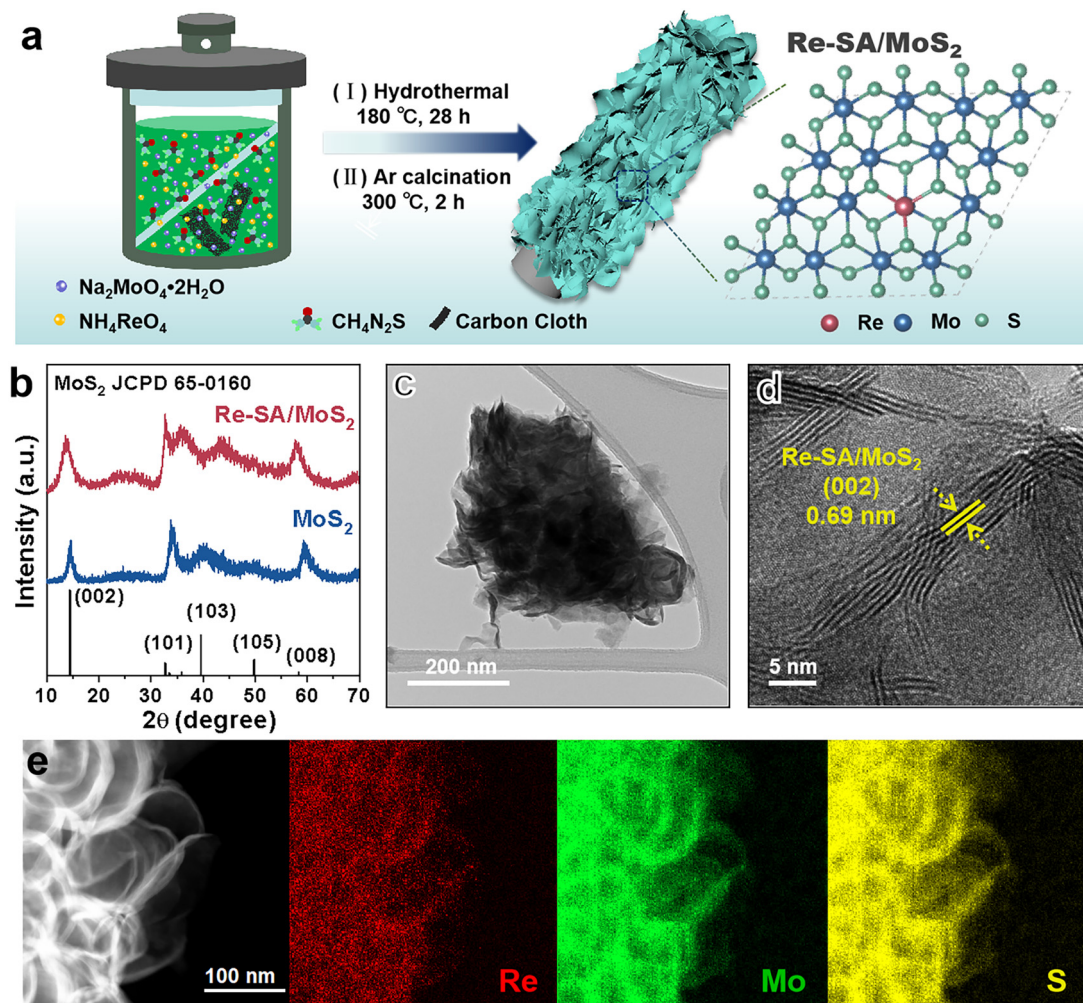
Fig. 1 (a) Schematic illustration of the fabrication of the Re−SA/MoS$_2$ catalysts. (b) XRD patterns of the fabricated MoS$_2$ and Re−SA/MoS$_2$ catalysts. (c and d) TEM and HRTEM images of the Re−SA/MoS$_2$ catalyst. (e) EDS mapping of the Re−SA/MoS$_2$ catalyst.

transition of MoS$_2$ from the 2H to the 1T phase could be achieved with the assistance of the Re SA.[31] Notably, the low vibrational mode intensity of E_{2g}^1 and 2H-A$_{1g}$ peak vanished in Re−SA/MoS$_2$, indicating that a high degree of the 1T-phase of MoS$_2$ was obtained. X-ray photoelectron spectroscopy (XPS) was also conducted to analyze the content of the 2H-to-1T crystal phase and surface chemical states of different elements. The full XPS spectra (Fig. S4a and b, ESI†) exhibited the existence of Re in the structure of MoS$_2$, and the surface Re concentration was calculated as 8.80 at% for Re−SA/MoS$_2$, in line with the EDS results (8.45 at% Re). As illustrated in Fig. S5a and b, ESI,† an apparent negative shift of 0.7 and 0.5 eV in the high-resolution XPS spectra of Mo 3d and S 2p of the Re−SA/MoS$_2$ nanosheets compared to the pristine MoS$_2$ moiety, suggests the formation of the 1T phase when the Re atom became accessed. The high-resolution Mo 3d spectra (Fig. 2g) of the Re−SA/MoS$_2$ and MoS$_2$ samples were divided into four typical peaks in terms of the standard deconvolution principles. The two peaks at 229.1 and 232.2 eV were attributed to Mo^{4+} 3d$_{5/2}$ and Mo^{4+} 3d$_{3/2}$ in 2H-phase MoS$_2$, respectively[32] while the two distinct peaks located at about 228.5 and 231.6 eV were present and attributed to 1T-phase MoS$_2$

according to previous works.[33] From the XPS results, the content of the 2H-phase-derived 1T phase of MoS$_2$ in Re−SA/MoS$_2$ was calculated to be about 85%, which can be ascribed to the Re atoms serving as electron donors within the lattice of MoS$_2$ and thereby resulting in the conversion of the 2H-phase to the 1T-phase *via* gliding of the atomic plane of S.[24,34] Besides, the two small peaks at 233.2 and 235.7 eV can be assigned to Mo^{6+} 3d$_{5/2}$ and Mo^{6+} 3d$_{3/2}$, implying that the MoS$_2$ surface undergoes partial oxidation in air.[35] Similarly, in the S 2p XPS spectra (Fig. 2h) of the Re−SA/MoS$_2$ and MoS$_2$ samples, two apparent peaks located at 163.1 eV and 161.9 eV correspond to S^{2-} 2p$_{1/2}$ and S^{2-} 2p$_{3/2}$, respectively. With the introduction of the Re species, the Re−SA/MoS$_2$ nanosheets revealed that the S 2p peaks change to a lower binding energy of about 162.7 eV for S^{2-} 2p$_{1/2}$ and 161.4 eV for S^{2-} 2p$_{3/2}$. This result also confirmed that the increase in the electronic density in MoS$_2$ was caused by the abundance of the 1T metallic phase.[36] Meanwhile, the Re 4f XPS spectrum of the Re−SA/MoS$_2$ sample exhibited a relatively high content of Re^{4+} 4f$_{5/2}$ and Re^{4+} 4f$_{7/2}$ oxidation states (Fig. 3a), implying that the local charge transfer occurred from the isolated Re atom to the adjacent S atom.[37]
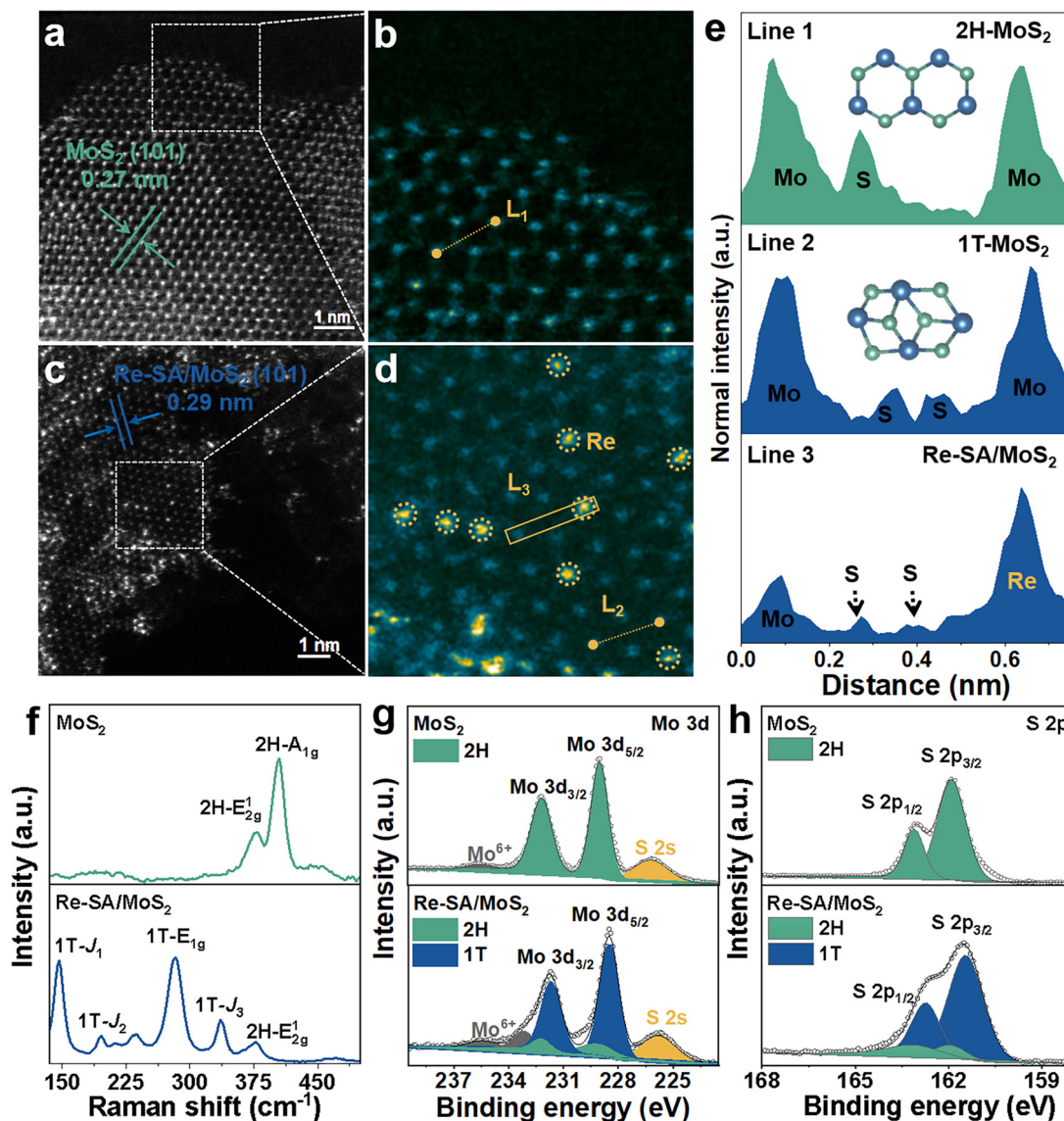
Fig. 2 (a and c) HAADF and (b and d) enlarged HAADF images of the 2H-MoS$_2$ and Re−SA/MoS$_2$ catalysts. (e) HAADF intensity line profiles taken along the numbered lines indicated in b and d. (f) Raman spectra of the fabricated MoS$_2$ and Re−SA/MoS$_2$ catalysts. (g and h) XPS spectra of the Mo 3d and S 2p of the fabricated MoS$_2$ and Re−SA/MoS$_2$ catalysts.

To verify the electronic state and local coordination environment of the Re atoms and Mo atoms in Re−SA/MoS$_2$, the X-ray absorption near edge structure (XANES) and extended X-ray absorption fine structure (EXAFS) measurements were further performed. In the Re L$_3$-edge XANES spectra (Fig. 3b), the intensity of the white line peak for Re−SA/MoS$_2$ is higher than that of the reference Re foil but lower than that of standard ReO$_2$, suggesting that the isolated Re atom has a valence between Re^0 (Re foil) and Re^{4+} (ReO$_2$), agreeing with the XPS results. Also the k^3-weighted Re L$_3$-edge Fourier-transformed EXAFS spectra (Fig. 3c) showed that the peak at 2.02 Å was attributed to the first Re−S shell in the spectrum of Re−SA/MoS$_2$. In comparison, the absence of a scattering peak at about 2.62 Å, derived from the Re−Re bond in the spectrum of Re foil, indicated the existence of the Re individual atoms rather than

Re clusters.[38] Additionally, the EXAFS fitting results (Fig. 3d and Table S1, ESI†) revealed the average coordination number about the central Re atoms to be 4.9 with a bond length of 2.37 Å for the Re−S scattering path, implying that Re atoms may exist as adsorption atoms or substitution within the MoS$_2$ lattice.[23,28] To observe the coordination information of Re sites in both k and R spaces, the wavelet transform (WT) of the Re L$_3$-edge EXAFS spectra (Fig. 3e and f) was explored. The maximum intensity of Re foil was 12.3 Å^{-1} in the k space, corresponding to a Re−Re scattering path. However, the maximum intensity for Re−SA/MoS$_2$ was observed around 6.6 Å^{-1} in the k space, demonstrating the formation of Re SA surrounded by S atoms, and Re atoms in Re−SA/MoS$_2$ were atomically dispersed. Furthermore, the enlarged Mo K-edge XANES spectra for Re−SA/MoS$_2$ (the inset in Fig. S6a, ESI†) were negatively
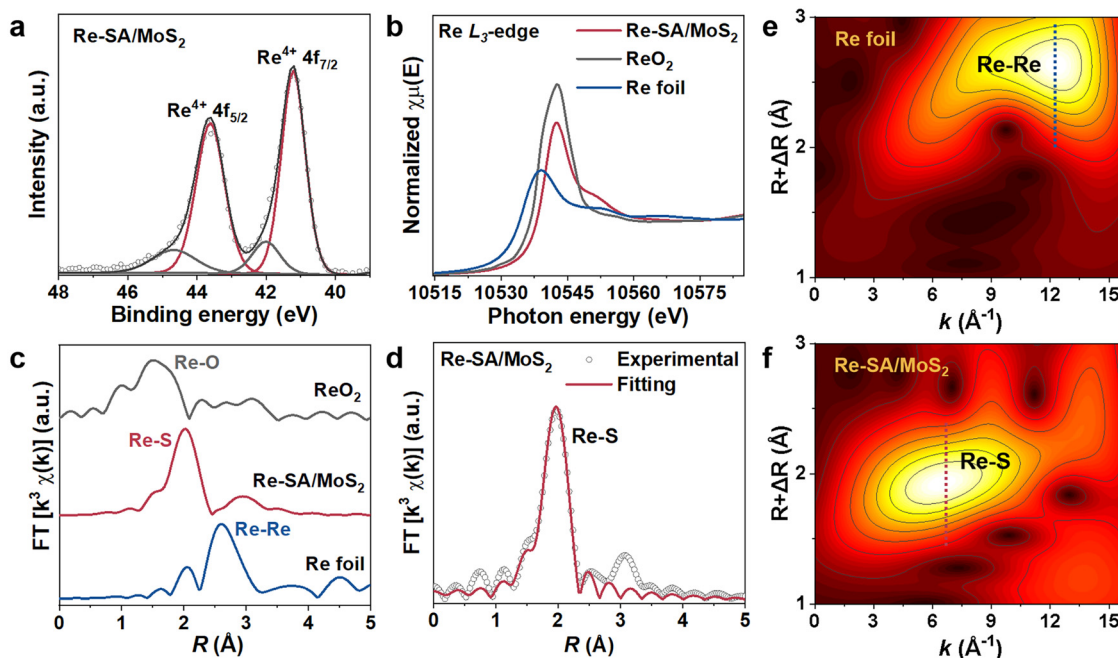
Fig. 3 (a) XPS spectrum of Re 4f in the Re−SA/MoS$_2$ catalyst. (b) XANES spectra of Re L$_3$-edge of Re foil, ReO$_2$ and Re−SA/MoS$_2$. (c) k^3-weighted Re L$_3$-edge Fourier-transformed EXAFS spectra for Re foil, ReO$_2$ and Re−SA/MoS$_2$. (d) EXAFS spectra (experimental and fitting) of Re L$_3$-edge of Re−SA/MoS$_2$. (e and f) Wavelet-transformation for Re L$_3$-edge of Re foil and Re−SA/MoS$_2$ in R space.

shifted compared to those of MoS$_2$, manifesting the strong interaction between MoS$_2$ and Re atoms in Re−SA/MoS$_2$. This was also reflected by the EXAFS spectroscopy and WT-EXAFS analysis of the Mo K-edge of MoS$_2$ and Re−SA/MoS$_2$ (Fig. S6 and Table S2, ESI†), which showed the two distinct peaks located at 1.99 and 2.88 Å attributed to Mo−S and Mo−Mo bonds (Fig. S6b, ESI†), respectively. Compared to MoS$_2$, the peak intensity of Mo−Mo coordination of the Re−SA/MoS$_2$ was reduced significantly, thus indicating a typical characteristic of 1T-phase MoS$_2$.[39] Based on these results, it could be speculated that the phase transformation and the electronic structure adjustment that occurred by incorporating the Re species into the lattice.[15]

Electrocatalytic performance toward the HER

The HER electrocatalytic activities were first performed in an alkaline media (1.0 M KOH), while MoS$_2$, Re−SA/MoS$_2$, and commercial Pt/C (20 wt%) were used as control samples. As depicted in Fig. 4a and b and Fig. S7a and b, ESI,† the *iR*-compensated linear sweep voltammetry (LSV) polarization curves displayed that the activity of the optimized Re−SA/MoS$_2$ only required overpotentials of 38 mV and 161 mV to reach the −10 mA cm^{-2} and −100 mA cm^{-2}, respectively, which are remarkably better than those observed for MoS$_2$ (191 and 323 mV), commercial Pt/C (54 and 251 mV), and comparable to that of the state-of-the-art MoS$_2$-based HER electrocatalysts (Table S3, ESI†). Additionally, the Tafel slope (Fig. 4c) of the MoS$_2$ without the incorporation of the Re SA exhibited a value of 104 mV dec^{-1}, much inferior to that of 66 mV dec^{-1} for the optimized Re−SA/MoS$_2$ (Fig. S7b and c, ESI†), implying that the HER typically followed the Volmer–Heyrovsky mechanism with water dissociation to H* and OH* as

the rate-determining step.[40] Electrochemical impedance spectroscopy (EIS) was further conducted to probe the charge-transfer dynamics in the HER process. As illustrated in Fig. S7d and Table S4, ESI,† the optimized Re−SA/MoS$_2$ catalysts possessed faster interfacial electron-transfer kinetics between the electrode and electrolyte, according to the smaller charge transfer resistance (R_{ct}) than the MoS$_2$ samples. Furthermore, the electrochemical HER performance was also measured in an acid media (0.5 M H$_2$SO$_4$). The LSV curves of the optimized Re−SA/MoS$_2$ catalysts delivered a significantly lower overpotential of 34 and 120 mV to reach −10 mA cm^{-2} and −100 mA cm^{-2} (Fig. 4d, e and Fig. S8a, b, ESI†), much superior to those of MoS$_2$ (166 and 317 mV) and commercial Pt/C (43 and 200 mV), and surpassing those of most of the previously reported MoS$_2$-based materials (Table S5, ESI†). The promising acidic HER activity of Re−SA/MoS$_2$ was further verified by the lower charge transfer resistance (R_{ct}) (Fig. S8c and Table S6, ESI†) with a more downward Tafel slope of 34 mV dec^{-1} compared to Pt/C (42 mV dec^{-1}) (Fig. 4f and Fig. S8d, ESI†), suggesting that the HER process on Re−SA/MoS$_2$ was accelerated by the rapid electron transfer kinetics and reduced energy barrier of the Volmer–Tafel step.[41] The electrochemical surface area (ECSA) of catalysts under acidic media was investigated through the use of double-layer capacities (C_{dl}) in Fig. S9a and b, ESI;† the favorable Re−SA/MoS$_2$ catalysts exhibited a higher ECSA value (Fig. S9c and d, ESI†) of 63 mF cm^{-2} than that of MoS$_2$ (11 mF cm^{-2}), confirming that the more plentiful active site was exposed through the implanted of Re SA for boosting the HER activity. The Re−SA/MoS$_2$ catalysts exhibited superior durability without any noticeable degradation after 25 h at ∼20 mA cm^{-2} and 23 mA cm^{-2} for HER in both alkaline and acidic electrolytes, respectively (Fig. 4g and h).
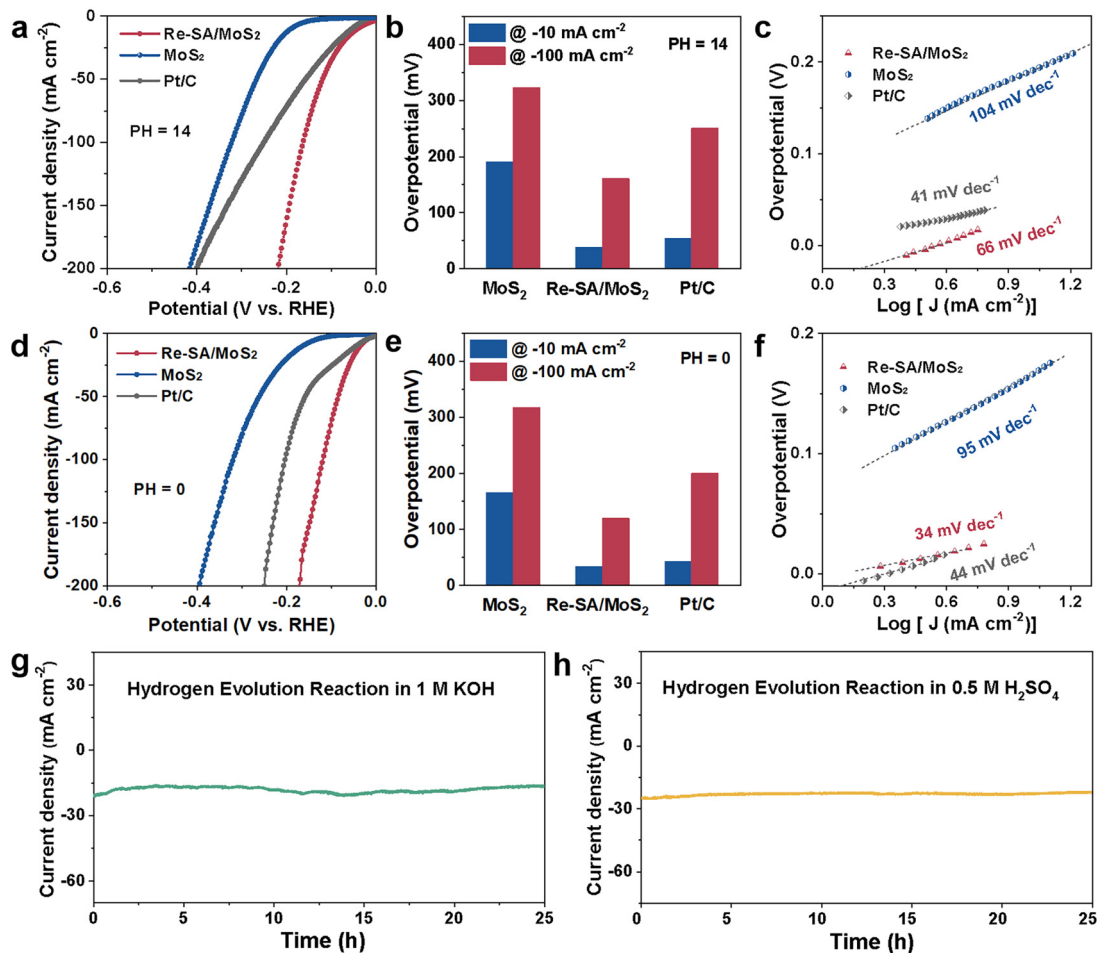
Fig. 4 HER performances of the Re−SA/MoS$_2$ electrocatalysts and control samples in H$_2$-saturated 1.0 M KOH: (a) LSV curves, (b) overpotentials at current densities of −10 and −100 mA cm^{-2}, and (c) Tafel plots toward HER. The HER performances of Re−SA/MoS$_2$ electrocatalysts and control samples in H$_2$-saturated 0.5 M H$_2$SO$_4$: (d) LSV curves, (e) overpotentials at current densities of −10 and −100 mA cm^{-2}, (f) Tafel plots toward HER. (g and h) Long-term cycling stability test of Re−SA/MoS$_2$ for HER in 1.0 M KOH and 0.5 M H$_2$SO$_4$, respectively.

In addition, there were no significant changes in the TEM, HRTEM, and EDS mapping results for the verification of the morphology (Fig. S10 and S11, ESI†), and the lattice structure and the content of 1T-phase, were maintained after the stability test (Fig. S12 and S13, ESI†).

Catalytic mechanisms

To unravel the underlying origin of superior HER catalytic activities with the Re atoms incorporated into MoS$_2$, the reaction Gibbs free energies profiles on HER of pure MoS$_2$ and Re−SA/MoS$_2$ have been deliberately assessed through first-principles DFT calculations. The constructed slab models for DFT calculations are illustrated in Fig. S14, ESI†. As shown, the Re atom was substituted at the Mo site or adsorbed on the Mo site via covalent bonds with S atoms, which are denoted as "Re$_{sub}$−SA/MoS$_2$" and "Re$_{ads}$−SA/MoS$_2$". Moreover, the pristine MoS$_2$ (2H-MoS$_2$) and the reference 1T-phase MoS$_2$ (1T-MoS$_2$) were also constructed for comparison. The optimized geometry structures with the adsorption intermediates (H$_2$O*, OH* + H*, and H*) of HER on 2H-MoS$_2$, 1T-MoS$_2$, Re$_{ads}$−SA/MoS$_2$, and Re$_{sub}$−SA/MoS$_2$ are shown in Fig. 5a and Fig.

S15, ESI.† As indicated in Fig. 5b, the introduction of Re atoms into MoS$_2$ triggers the water hydrolysis reaction with a significantly lower energy barrier (−0.22 eV) than pure MoS$_2$ (3.52 eV), thereby accelerating the water splitting. This much easier water association on newly implanted Re atoms of Re−SA/MoS$_2$ facilitates faster proton supply for the subsequent HER process. Calculated free energy changes of adsorbed hydrogen (ΔG_{H*}) on possible active sites as key descriptors for evaluating HER electrocatalysis are illustrated in Fig. 5c, from which it is apparent that the highest HER activity is strongly associated with the absolute value of ΔG_{H*} close to zero.[42] Our results reveal that the ΔG_{H*} values of Re$_{ads}$−SA/MoS$_2$ on the S site (−0.2 eV) are much closer to the optimal value than those of pure 2H-MoS$_2$ on the S site (2.1 eV), pure 1T-MoS$_2$ on S site (0.8 eV), and Re$_{sub}$−SA/MoS$_2$ on S site (−0.8 eV), implying that the integration of Re atoms could redistribute electronic structures and thus optimize the H adsorption/ desorption on the MoS$_2$ surface.

Furthermore, the corresponding differential charge density distribution and density of state (DOS) were simulated for investigating the intrinsic activity of Re−SA/MoS$_2$ and elucidating the
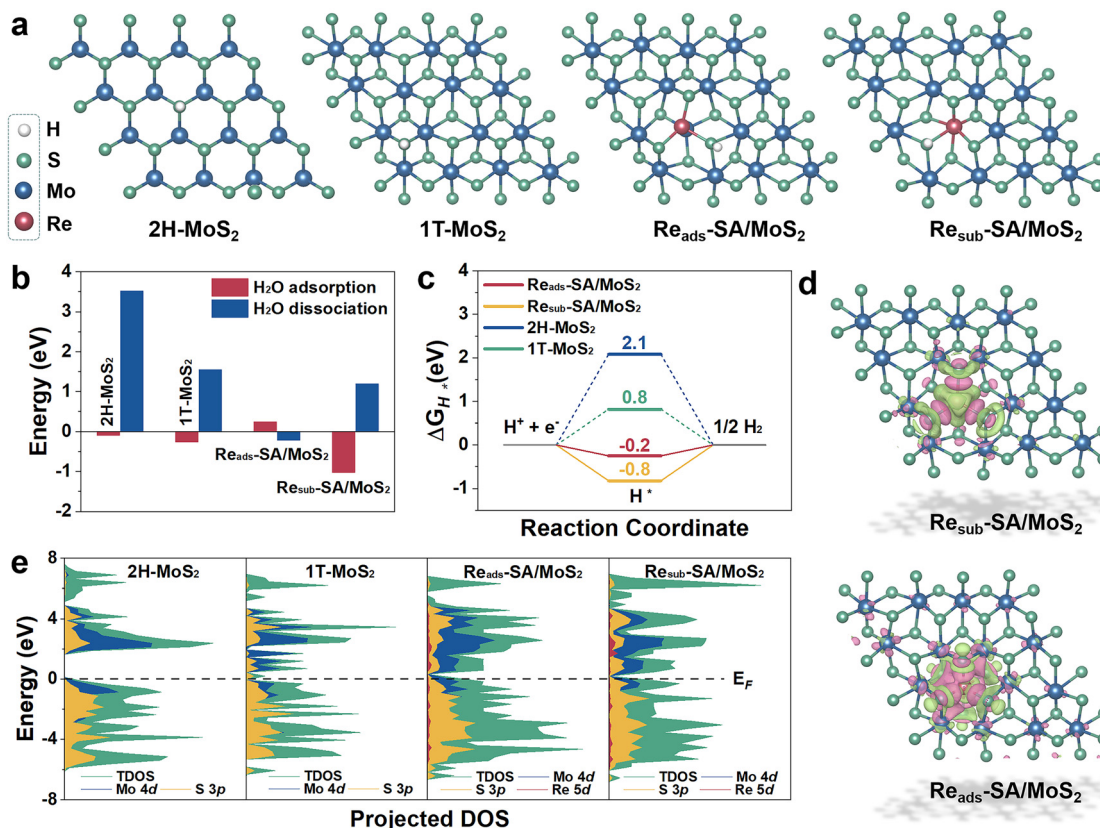
Fig. 5 Theoretical calculations on the HER. (a) Atomic structures (top views) of the optimized slabs in 2H-MoS$_2$, 1T-MoS$_2$ and two Re doping configurations. (b) Calculated adsorption/dissociation energy of H$_2$O for hydrogen evolution reaction on the 2H-MoS$_2$, 1T-MoS$_2$, Re$_{ads}$–SA/MoS$_2$ and Re$_{sub}$–SA/MoS$_2$ surface. (c) Free energy diagram of 2H-MoS$_2$, 1T-MoS$_2$, Re$_{ads}$–SA/MoS$_2$ and Re$_{sub}$–SA/MoS$_2$ for HER. (d) Differential charge density distributions of Re$_{ads}$–SA/MoS$_2$ and Re$_{sub}$–SA/MoS$_2$. The green and purple areas represent electron accumulation and depletion, respectively. (e) Projected DOS of 2H-MoS$_2$, 1T-MoS$_2$, Re$_{ads}$–SA/MoS$_2$ and Re$_{sub}$–SA/MoS$_2$.

effect of distinct electronic structures and activity in the HER. As exhibited in Fig. 5d, the significant differential charge density occurs around Re–S bonds after the Re atoms substitute/adsorption in the Mo atoms, meaning that introducing Re atoms into MoS$_2$ can remarkably adjust the sample's electronic structure. Additionally, the electronic characteristic of the different samples is further indicated according to the corresponding DOS (Fig. 5e). The pristine 1T-MoS$_2$ and Re–SA/MoS$_2$ possess an inherent metallic nature. Intriguingly, the introduction of Re atoms into MoS$_2$ triggers the computing DOS to become more pronounced around the Fermi level (E_f) as compared to MoS$_2$ due to the hybridization of Re 5d with Mo 4d and S 3p orbitals, indicating more increased metallic features and higher electrical conductivity on the Re–SA/MoS$_2$ catalysts than the pure 2H-MoS$_2$, leading to more efficient electrochemical reactions. This electronic behavior thus reveals that introducing the Re SA could result in local charge redistribution and modulate the electronic structure of 2H-MoS$_2$ to improve the hydrogen evolution performance.

85%) of MoS$_2$ from the 2H-phase to the 1T-phase for improving the catalytic HER performance. The optimized Re–SA/MoS$_2$ exhibited a Pt-like HER performance, with an overpotential of 34 mV and 38 mV at a current density of -10 mA cm^{-2} in both acidic and alkaline media, much superior to that of pristine MoS$_2$ and comparable to that of the state-of-the-art Pt/C. The considerable enhancement of catalytic activity for the Re–SA/MoS$_2$ nanosheets could be ascribed to the following reasons. First, the conductivity properties of MoS$_2$ were improved by an electron injection effect of the single atom Re for modulating the lattice structure of 2H-MoS$_2$ to promote phase conversion to the 1T phase. Second, single-atom Re acted as a catalytic site, effectively accelerating the water dissociation kinetics. Third, the adsorption of the H intermediate with the energy barrier of the rate-determining step was reduced by the strong synergistic between Re–SA and MoS$_2$, further facilitating the subsequent H$_2$ generation. In short, this work's phase transition with a single-atom engineering strategy will enrich the design of advanced HER catalysts and has broad applicability for other catalytic systems.

Conclusions

In summary, we have successfully demonstrated that the introduction of single-atom Re on MoS$_2$ induced the phase transition (ca.

Author contributions

Conceptualization: J. Y., T. Z., L. S., and H. L. Methodology: J. Y., Y. Q., Q. W., and L. S. Formal analysis: J. Y. and Y. Q.

Investigation: J. Y., Y. Q., and Q. W. Visualization: J. Y. and L. S. Supervision: C. S., L. S., and T. Z. Writing – original draft: J. Y., and L. S. Writing – review and editing: J. Y., C. S., H. Y., L. S., and T. Z.

Conflicts of interest

There are no conflicts to declare.

Acknowledgements

Notes and references

1 X. Wang, Y. Zhang, J. Wu, Z. Zhang, Q. Liao, Z. Kang and Y. Zhang, *Chem. Rev.*, 2022, **122**, 1273–1348.
2 J. Yu, T. A. Le, N. Q. Tran and H. Lee, *Chem. – Eur. J.*, 2020, **26**, 6423–6436.
3 W.-H. Lai, L.-F. Zhang, W.-B. Hua, S. Indris, Z.-C. Yan, Z. Hu, B. Zhang, Y. Liu, L. Wang, M. Liu, R. Liu, Y.-X. Wang, J.-Z. Wang, Z. Hu, H.-K. Liu, S.-L. Chou and S.-X. Dou, *Angew. Chem., Int. Ed.*, 2019, **58**, 11868–11873.
4 Y. Li, Y. Sun, Y. Qin, W. Zhang, L. Wang, M. Luo, H. Yang and S. Guo, *Adv. Energy Mater.*, 2020, **10**, 1903120.
5 S. Zhang, X. Zhang, Y. Rui, R. Wang and X. Li, *Green Energy Environ.*, 2021, **6**, 458–478.
6 S. Manzeli, D. Ovchinnikov, D. Pasquier, O. V. Yazyev and A. Kis, *Nat. Rev. Mater.*, 2017, **2**, 17033.
7 Q. Fu, J. Han, X. Wang, P. Xu, T. Yao, J. Zhong, W. Zhong, S. Liu, T. Gao, Z. Zhang, L. Xu and B. Song, *Adv. Mater.*, 2021, **33**, 1907818.
8 Y. Cao, *ACS Nano*, 2021, **15**, 11014–11039.
9 Q. Tang and D. Jiang, *ACS Catal.*, 2016, **6**, 4953–4961.
10 M. A. Lukowski, A. S. Daniel, F. Meng, A. Forticaux, L. Li and S. Jin, *J. Am. Chem. Soc.*, 2013, **135**, 10274–10277.
11 J. Zhu, Z. Wang, H. Yu, N. Li, J. Zhang, J. Meng, M. Liao, J. Zhao, X. Lu, L. Du, R. Yang, D. Shi, Y. Jiang and G. Zhang, *J. Am. Chem. Soc.*, 2017, **139**, 10216–10219.
12 Z. Liu, K. Nie, X. Qu, X. Li, B. Li, Y. Yuan, S. Chong, P. Liu, Y. Li, Z. Yin and W. Huang, *J. Am. Chem. Soc.*, 2022, **144**, 4863–4873.
13 S. Wang, D. Zhang, B. Li, C. Zhang, Z. Du, H. Yin, X. Bi and S. Yang, *Adv. Energy Mater.*, 2018, **8**, 1801345.
14 S. Jiménez Sandoval, D. Yang, R. F. Frindt and J. C. Irwin, *Phys. Rev. B: Condens. Matter Mater. Phys.*, 1991, **44**, 3955–3962.
15 S. Wei, X. Cui, Y. Xu, B. Shang, Q. Zhang, L. Gu, X. Fan, L. Zheng, C. Hou, H. Huang, S. Wen and W. Zheng, *ACS Energy Lett.*, 2018, **4**, 368–374.
16 X. Meng, C. Ma, L. Jiang, R. Si, X. Meng, Y. Tu, L. Yu, X. Bao and D. Deng, *Angew. Chem., Int. Ed.*, 2020, **59**, 10502–10507.
17 Z. Luo, H. Zhang, Y. Yang, X. Wang, Y. Li, Z. Jin, Z. Jiang, C. Liu, W. Xing and J. Ge, *Nat. Commun.*, 2020, **11**, 1116.
18 T. Rao, H. Wang, Y.-J. Zeng, Z. Guo, H. Zhang and W. Liao, *Adv. Sci.*, 2021, **8**, 2002284.
19 J. Zhang, X. Xu, L. Yang, D. Cheng and D. Cao, *Small Methods*, 2019, **3**, 1900653.
20 Y. Li, Q. Gu, B. Johannessen, Z. Zheng, C. Li, Y. Luo, Z. Zhang, Q. Zhang, H. Fan, W. Luo, B. Liu, S. Dou and H. Liu, *Nano Energy*, 2021, **84**, 105898.
21 K. Zhang, B. M. Bersch, J. Joshi, R. Addou, C. R. Cormier, C. Zhang, K. Xu, N. C. Briggs, K. Wang, S. Subramanian, K. Cho, S. Fullerton-Shirey, R. M. Wallace, P. M. Vora and J. A. Robinson, *Adv. Funct. Mater.*, 2018, **28**, 1706950.
22 S.-Z. Yang, Y. Gong, P. Manchanda, Y.-Y. Zhang, G. Ye, S. Chen, L. Song, S. T. Pantelides, P. M. Ajayan, M. F. Chisholm and W. Zhou, *Adv. Mater.*, 2018, **30**, 1803477.
23 X. Tian, D. S. Kim, S. Yang, C. J. Ciccarino, Y. Gong, Y. Yang, Y. Yang, B. Duschatko, Y. Yuan, P. M. Ajayan, J. C. Idrobo, P. Narang and J. Miao, *Nat. Mater.*, 2020, **19**, 867–873.
24 A. N. Enyashin, L. Yadgarov, L. Houben, I. Popov, M. Weidenbach, R. Tenne, M. Bar-Sadan and G. Seifert, *J. Phys. Chem. C*, 2011, **115**, 24586–24591.
25 Y. Sun, Y. Zang, W. Tian, X. Yu, J. Qi, L. Chen, X. Liu and H. Qiu, *Energy Environ. Sci.*, 2022, **15**, 1201–1210.
26 A. Kumar, X. Liu, J. Lee, B. Debnath, A. R. Jadhav, X. Shao, V. Q. Bui, Y. Hwang, Y. Liu, M. G. Kim and H. Lee, *Energy Environ. Sci.*, 2021, **14**, 6494–6505.
27 Y. C. Lin, D. O. Dumcenco, H. P. Komsa, Y. Niimi, A. V. Krasheninnikov, Y. S. Huang and K. Suenaga, *Adv. Mater.*, 2014, **26**, 2857–2861.
28 I. S. Kwon, I. H. Kwak, S. Ju, S. Kang, S. Han, Y. C. Park, J. Park and J. Park, *ACS Nano*, 2020, **14**, 12184–12194.
29 J. Deng, H. Li, J. Xiao, Y. Tu, D. Deng, H. Yang, H. Tian, J. Li, P. Ren and X. Bao, *Energy Environ. Sci.*, 2015, **8**, 1594–1601.
30 X. Geng, W. Sun, W. Wu, B. Chen, A. Al-Hilo, M. Benamara, H. Zhu, F. Watanabe, J. Cui and T. Chen, *Nat. Commun.*, 2016, **7**, 10672.
31 Y. Fang, J. Pan, J. He, R. Luo, D. Wang, X. Che, K. Bu, W. Zhao, P. Liu, G. Mu, H. Zhang, T. Lin and F. Huang, *Angew. Chem., Int. Ed.*, 2018, **57**, 1232–1235.
32 Z. Li, C. Li, J. Chen, X. Xing, Y. Wang, Y. Zhang, M. Yang and G. Zhang, *J. Energy Chem.*, 2022, **70**, 18–26.
33 Y. Yu, G.-H. Nam, Q. He, X.-J. Wu, K. Zhang, Z. Yang, J. Chen, Q. Ma, M. Zhao, Z. Liu, F.-R. Ran, X. Wang, H. Li, X. Huang, B. Li, Q. Xiong, Q. Zhang, Z. Liu, L. Gu, Y. Du, W. Huang and H. Zhang, *Nat. Chem.*, 2018, **10**, 638–643.
34 Y.-C. Lin, D. O. Dumcenco, Y.-S. Huang and K. Suenaga, *Nat. Nanotechnol.*, 2014, **9**, 391–396.
35 G. Wang, G. Zhang, X. Ke, X. Chen, X. Chen, Y. Wang, G. Huang, J. Dong, S. Chu and M. Sui, *Small*, 2022, **18**, 2107238.

36 M. Liu, J.-A. Wang, W. Klysubun, G.-G. Wang, S. Sattayaporn, F. Li, Y.-W. Cai, F. Zhang, J. Yu and Y. Yang, *Nat. Commun.*, 2021, **12**, 5260.

37 Y. Shi, Z.-R. Ma, Y.-Y. Xiao, Y.-C. Yin, W.-M. Huang, Z.-C. Huang, Y.-Z. Zheng, F.-Y. Mu, R. Huang, G.-Y. Shi, Y.-Y. Sun, X.-H. Xia and W. Chen, *Nat. Commun.*, 2021, **12**, 3021.

38 Z. Li, X. Yan, D. He, W. Hu, S. Younan, Z. Ke, M. Patrick, X. Xiao, J. Huang, H. Wu, X. Pan and J. Gu, *ACS Catal.*, 2022, **12**, 7687–7695.

39 Q. Liu, X. Li, Q. He, A. Khalil, D. Liu, T. Xiang, X. Wu and L. Song, *Small*, 2015, **11**, 5556–5564.

40 Y. Yin, J. Han, Y. Zhang, X. Zhang, P. Xu, Q. Yuan, L. Samad, X. Wang, Y. Wang, Z. Zhang, P. Zhang, X. Cao, B. Song and S. Jin, *J. Am. Chem. Soc.*, 2016, **138**, 7965–7972.

41 Z. Zheng, L. Yu, M. Gao, X. Chen, W. Zhou, C. Ma, L. Wu, J. Zhu, X. Meng, J. Hu, Y. Tu, S. Wu, J. Mao, Z. Tian and D. Deng, *Nat. Commun.*, 2020, **11**, 3315.

42 X. Zhang, A. Chen, L. Chen and Z. Zhou, *Adv. Energy Mater.*, 2022, **12**, 2003841.